Spin-valve-like magnetoresistance and anomalous Hall effect in magnetic Weyl metal Mn_2PdSn

Arnab Bhattacharya,[1] Mohammad Rezwan Habib,[2] Afsar Ahmed,[1] Biswarup Satpati,[1] Samik DuttaGupta,[1] Indra Dasgupta,[2,*] and I. Das[1,†]

[1]*Condensed Matter Physics Division, Saha Institute of Nuclear Physics, A CI of Homi Bhabha National Institute, 1/AF, Bidhannagar, Kolkata 700064, India*

[2]*School of Physical Sciences, Indian Association for the Cultivation of Science, 2A and 2B Raja S.C. Mullick Road, Jadavpur, Kolkata 700 032, India*

(Received 1 April 2024; revised 21 May 2024; accepted 20 June 2024; published 11 July 2024)

Realization of noncentrosymmetric magnetic Weyl metals is expected to exhibit anomalous transport properties stemming from the interplay of unusual bulk electronic topology and magnetism. Here, we present spin-valve-like magnetoresistance at room temperature in ferrimagnetic Weyl metal Mn_2PdSn that crystallizes in the inverse Heusler structure. Anomalous magnetoresistance displays dominant asymmetric component attributed to domain wall electron scattering, indicative of spin-valve-like behavior. *Ab initio* calculations confirm the topologically nontrivial nature of the band structure, with Weyl nodes proximate to Fermi energy, providing deeper insights into the observed intrinsic Berry curvature mediated substantial anomalous Hall conductivity. Our results underscore the inverse Heusler compounds as promising platform to realize magnetic Weyl metals/semimetals and leverage emergent transport properties for electronic functionalities.

DOI: 10.1103/PhysRevB.110.014417

In the landscape of condensed matter physics, there has been a fervent pursuit of discovering novel quantum materials, aiming to validate topological principles and unravel their associated exotic properties [1–4]. Among these, Weyl semimetals/metals (WSM) appear as a distinct class, emerging in crystals with broken inversion ($\mathcal{P}$) [5,6] or time-reversal ($\mathcal{T}$) symmetry [7–9], hosting bulk emergent Weyl fermions [10,11] and surface Fermi arcs connecting Weyl nodes of opposite chirality [12,13]. Notably the magnetic Weyl semimetals (MWSM) with broken $\mathcal{T}$ offer an expanded realm to explore the interplay between topological ordering, magnetism and electron correlation compared to their nonmagnetic counterparts [9–11]. In $\mathcal{P}$-conserved MWSMs, the broken-$\mathcal{T}$ induced persistent Berry curvature along with intrinsic magnetism results in remarkably large anomalous Hall conductivity (AHC) [13–17] and anomalous Hall angle [9,10], positioning MWSMs favourably for potential applications in spintronics. However, research in MWSMs has primarily focused on ferromagnets, where topological features are protected by mirror symmetry under conserved $\mathcal{P}$, subject to breakdown upon the inclusion of spin-orbit coupling (SOC). This limits the concurrent realization of real-space noncollinear magnetic ordering, such as skyrmions [18,19] or spin-valve effect [20–22], and nontrivial k-space topology, hindering exploration of the novel magnetic responses and valuable insights this synergy may offer.

In this context, 4d-transition-element-based inverse Heusler alloys (iHA) present an intriguing platform with noncentrosymmetric crystal structures and multiple inequivalent magnetic sublattices [23]. The advantages of 4d-transition metal-based alloys over extensively studied 3d counterparts lie in reduced antisite disorder, resulting from differences in size and electronegativity with other constituent elements, and enhanced SOC effects. The inherent magnetism of iHA lifts the band spin degeneracy, while moderate $\mathcal{P}$ breaking preserves the topological nature of the Weyl nodes, shifting them to different energies from the Fermi level. This shift eliminates the possibility of nodal semimetals while maintaining Weyl semimetal properties, such as chiral anomaly and large AHC [24]. In real-space scenario, the multiple magnetic sublattices introduce an additional layer of intricacy. The ferrimagnetism in majority of cubic Mn-based iHA arises from the antiferromagnetic coupling between Mn atoms in the tetragonal environment and highly localized octahedrally coordinated Mn atoms [25–27], exhibiting emergent phenomena such as exchange bias [28] and the rare spin-valve effect [20–22], serving a novel backdrop to explore the relation of Weyl fermions and magnetism.

Here we present Mn_2PdSn as candidate Weyl metal demonstrating room-temperature spin-valve-like magnetoresistance and substantial AHC, through combined experimental and theoretical study. Isothermal field-dependent longitudinal resistivity exhibits anomalous magnetoresistance (MR) dominated by asymmetric component indicating rare spin-valve behavior in stoichiometric systems. *Ab initio* calculations confirm the presence of Weyl points close to the Fermi level offering deeper insights into the Berry curvature mediated intrinsic AHC. We present a nontrivial AHC in the compensated ferrimagnetic Mn_2PdSn by determining the magnetic space group, which contains magnetic mirror planes. These results underscore iHA as a platform for simultaneous realization of nontrivial magnetic functionalities and electronic topology.

*Contact author: sspid@iacs.res.in
†Contact author: indranil.das@saha.ac.in

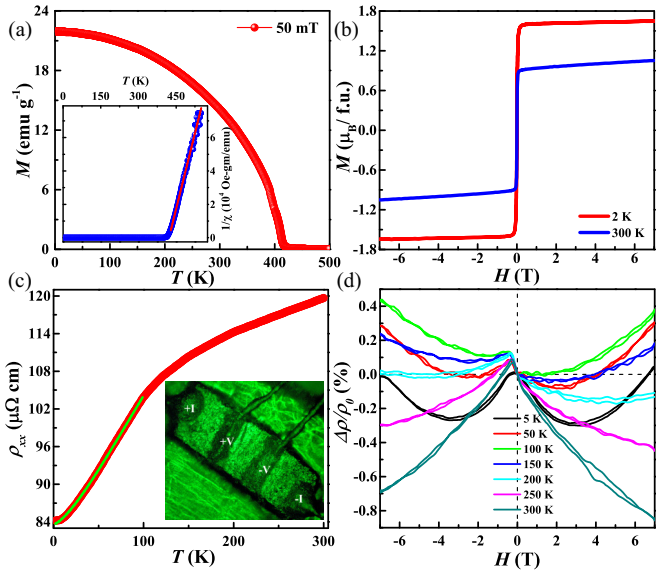

FIG. 1. (a) Temperature variation of magnetization under the applied field of 50 mT. The inset shows the inverse susceptibility curve versus temperature. (b) Isothermal magnetization $M(H)$ at 2 K and 300 K. (c) Temperature variation of ρ_{xx} with the green lines showing the fitted data. Inset image shows the sample contacts for longitudinal magnetotransport measurement. (d) Magnetic field dependance of isothermal magnetoresistance ($\Delta\rho/\rho_0$) at different temperatures.

Polycrystalline ingots of Mn_2PdSn were prepared by a conventional arc-melting technique (see Supplemental Material (SM) [29]). The compound crystallized in iHA structure (space group $F\bar{4}3m$) with a stoichiometric representation $XYX'Z$, where X, Y, X', and Z occupies the 4*c*, 4*d*, 4*b*, and 4*a* Wyckoff sites, respectively, across four interpenetrating FCC sublattices [30,31]. Selected area electron diffraction pattern (SAED) along the [110] zone axis and inverse fast Fourier transformation of the high-resolution TEM image of the samples, reveals the high crystal quality (see Fig. SF1 of SM [29]).

Like the majority of Mn_2-based iHA, thermomagnetic measurements $M(T)$ under an applied field of 50 mT reveal a paramagnetic to ferromagnetic (FM)/ferrimagnetic (FiM) transition above room temperature for Mn_2PdSn at $T_C =$ 410 K [Fig. 1(a)]. The susceptibility χ follows the Curie-Weiss (CW) law with $\theta_{CW} \approx 421.5$ K [inset of Fig. 1(a)]. The isothermal magnetization $M(H)$ at 2 K and 300 K reflects a soft FM/FiM nature with negligible hysteresis [Fig. 1(b)]. For iHA, the net magnetic moment follows the Slater-Pauling (SP) rule as $M_{sat} = (N_v - 24)\mu_B$/ f.u., where N_v is the total number of valence electrons [23]. Interestingly, from $M(H)$ isotherm at $T = 2$ K, we obtain a spontaneous moment of 1.62 μ_B/f.u., significantly lower than the SP rule estimate for complete FM ordering ($M_{sat} = 4\ \mu_B$/f.u, $N_v = 28$). This difference is attributed to the intersublattice antiferromagnetic correlation between octahedrally coordinated Mn_{4b} atoms in the Mn-Sn plane and Mn_{4c} at the tetrahedral site in Mn-Pd sublattice, resulting in net FiM ordering [25–28,41].

Figure 1(c) shows the temperature variation of longitudinal resistivity ρ_{xx} exhibiting a metallic behavior. To elucidate the dominant scattering mechanism in ρ_{xx}, we fit $\rho_{xx}(T)$ between 2 and 100 K using the *e-e* scattering T^2 dependence. However, a more accurate low-temperature fit incorporates the spin-fluctuating $T^{3/2}$ term, yielding $\rho_{xx} = \rho_0 + AT^{3/2} + BT^2$, where ρ_0 is residual resistivity, and A and B are constants [42,43]. The fitting results in $\rho_0 = 83.615$ μΩcm, $A = 3.442 \times 10^{-2}$ μΩcmK^{-1}, and $B = 1.39 \times 10^{-3}$μΩcmK^{-2}, highlighting the prominent role of spin fluctuation at low temperatures. This underscores that the interaction between conduction electrons and localized moments is not a weak perturbation but a strong electron-magnon interaction [44].

The magnetic field dependence of MR isotherms [$\Delta\rho/\rho_0 = \frac{\rho_{xx}(H)-\rho_{xx}(H=0)}{\rho_{xx}(H=0)} \times 100\%$] typically exhibits symmetry concerning the applied H direction. Conversely in Fig. 1(d) Mn_2PdSn exhibits distinct asymmetry around $H = 0$ upon field reversal across the entire T range, with the asymmetry along the initially applied field direction while the curve retraces when field is swept in opposite direction, reminiscent of magnetic-spin-valve behavior [20,21]. The asymmetric component of the MR defined as, $MR^{asm} = [MR(H) - MR(-H)]/2$, showcase a persistent presence from 5–300 K (see Fig. SF3(b) of SM [29]). MR^{asm} closely mirrors the $M(H)$ curves, underscoring the predominant influence of the change in magnetic ordering at low H within the magnetic domains on MR^{asm}. Intuitively, MR^{asm} can be attributed to the domain wall induced spin-dependant scattering of conduction electrons. The electrons follow a least-resistive path stemming from unidirectional spins within FM clusters embedded in FiM matrix with oppositely orientated moments at the domain walls, experiencing frustrated state, acts as pinning centers. This magnetic arrangement results in two distinct resistivity states, reflected as the spin-valve behavior in MR upon H reversal in low field region, sustained even at room temperature. Similar underlying mechanism originating from antisite disorder governs the spin-valve-like magnetoresistance in quaternary FeRhCrSi [20] and tetragonal Mn_2NiGa [21] Heusler alloys. To elucidate the temperature evolution of *MR* [Fig. 1(d)], we separate the symmetric component $MR^{sym} = [MR(H) + MR(-H)]/2$ (see Fig. SF3(a) of SM [29]). At lower T, MR^{sym} exhibits a positive slope for $H \geqslant$ 3 T, attributed to the Lorenz force acting on the conduction electrons. In contrast, the negative MR^{sym} at high T originates from the suppression of spin scattering with the application of H [45]. Thus establishing a close correlation between magnetism and transport properties.

Now we turn to Hall transport data. Figure 2(a) shows the transverse resistivity ρ_{xy} vs H at various T. For FM/FiM conductors, the ρ_{xy} can be empirically expressed as, $\rho_{xy} = \rho_{xy}^O + \rho_{xy}^A$, where $\rho_{xy}^O = R_0H$ and $\rho_{xy}^A = R_SM$ are ordinary and anomalous Hall resistivity, respectively [13–15]. The negative slope establishes electrons as the majority charge carriers with carrier density $n_0 = 7.8 \times 10^{21}$ cm^{-3} at $T = 2$ K. ρ_{xy}^A is obtained from high-H extrapolation to zero field, displaying an increasing trend with temperature [Fig. 2(b)], contrary to the behavior of M_s. In a generalized picture, the AHE stems from either intrinsic mechanism mediated by reciprocal space Berry curvature or extrinsic side-jump (sj)/skew (sk) scattering mechanisms [46]. To scrutinize the origin, we derive the AHC σ_{xy}^A, akin to obtaining ρ_{xy}^A, from total Hall conductivity $\sigma_{xy} \approx \rho_{xy}/\rho_{xx}^2$. σ_{xy}^A exhibits nearly constant variation with T,

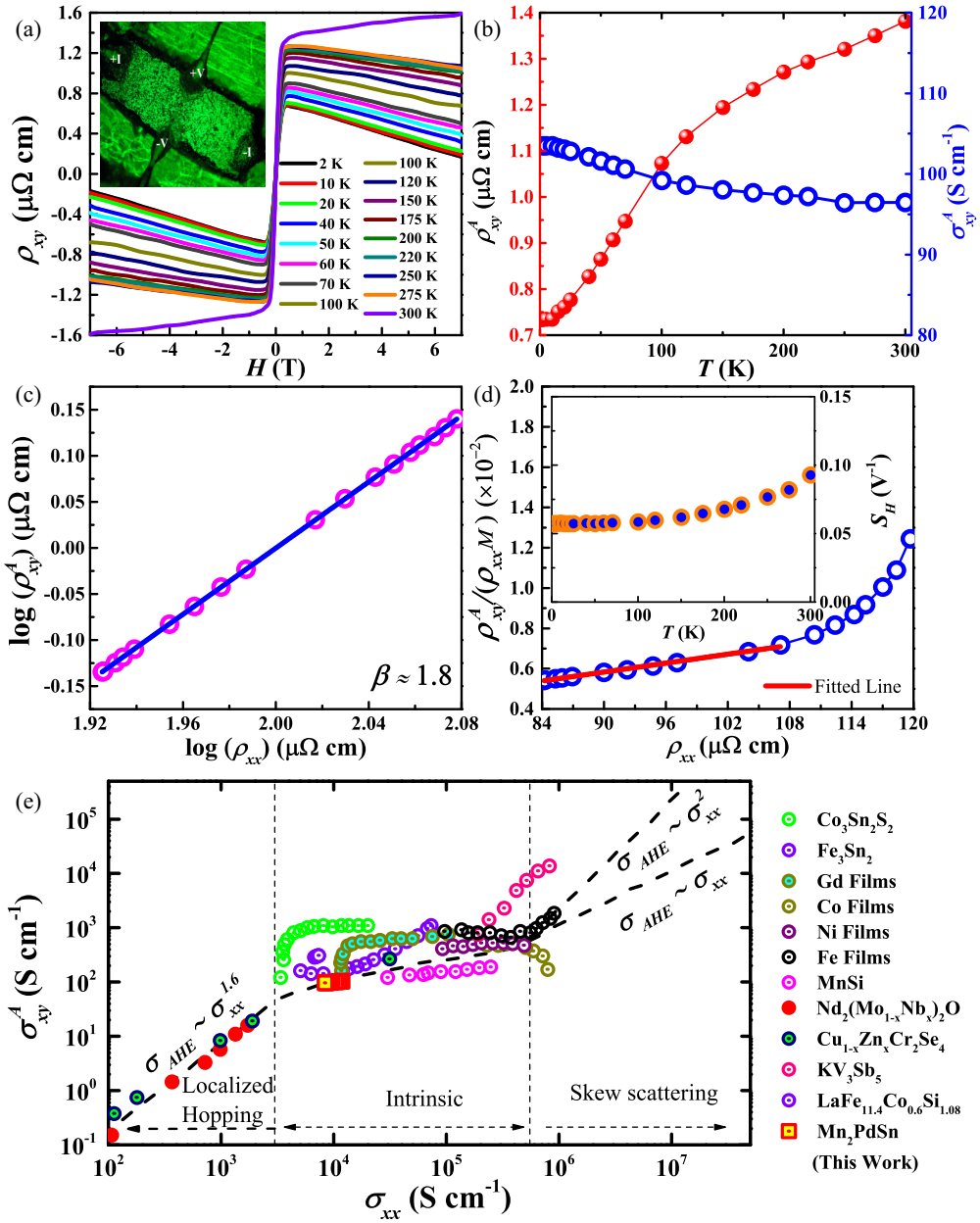

FIG. 2. (a) Isothermal transverse resistivity (ρ_{xy}) from 2–300 K. Inset shows the four-probe Hall contacts. (b) Temperature variation of anomalous Hall resistivity, ρ^A_{xy} and conductivity, σ^A_{xy}. (c) Plot of log(ρ^A_{xy}) vs log(ρ_{xx}) with the slope $\beta \approx 1.8$ (d) *TYJ* scaling of Hall resistivity. Inset shows the T variation of $S_H = \sigma^A_{xy}/M_S$. (f) Universal plot for σ^A_{xy} with σ_{xx} showing the intrinsic regime for Mn_2PdSn with earlier reported materials (in Fig. SF5 of Supplemental Material (SM) [29]), [13,17,32–40].

with a value of $\sigma^A_{xy} \approx 103.5$ Scm^{-1} at $T = 2$ K, suggesting an intrinsic origin of AHE [Fig. 2(b)] [8,9,35]. In Fig. 2(c), the linear relation between log(ρ^A_{xy}) and log(ρ_{xx}) is fitted using the relation $\rho^A_{xy} \propto \rho^{\beta}_{xx}$, which yields $\beta \approx 1.79(4)$, suggestive of the dominant contribution of intrinsic Berry curvature or extrinsic *sj* mechanism in AHE [47]. To quantify these contributions, we adopt the TYJ scaling relation [48], $\rho^A_{xy}/\rho_{xx}M = a + b\rho_{xx}$, where the first term a stems from extrinsic sk mechanism and the second term, $b = \rho^A_{xy}/\rho^2_{xx}$, relates directly with intrinsic AHC, $\sigma^A_{xy,\mathrm{int}}$. From the scaling, a linear relation is expected between $\rho^A_{xy}/(\rho_{xx}M)$ and ρ_{xx}, which prevails for $\rho_{xx} \leqslant 108$ μΩcm (corresponding to $T = 140$ K) resulting in $a \approx -8.1 \pm 2 \times 10^{-4}$ and $b \approx 74 \pm 3$ S cm^{-1} [Fig. 2(d)]. The observed $\sigma^A_{xy,\mathrm{int}}$ is comparable to several Co-based ferromagnetic Weyl semimetallic Heusler alloys [36,40,49]. The $\sigma^A_{xy,\mathrm{int}}$ accounts to 70% of σ^A_{xy} at $T = 2$ K. At low temperatures with reduced phonon scattering, the σ^A_{sj} entangles with $\sigma^A_{xy,\mathrm{int}}$, posing a challenge for individual quantification due to the absence of a scaling framework. However, an estimation of the order of magnitude of σ^A_{sj} [32] reveals it to be notably smaller than $\sigma^A_{xy,\mathrm{int}}$, thereby confirming the Karplus-Lüttinger origin of AHC [46].

Figure 2(e) shows the σ^A_{xy} versus σ_{xx} plot along with other known FM/FiM where it lies well within the limit for the

intrinsic origin of AHE. To gauge the robustness of AHE, we employ the anomalous Hall factor S_H ($= \sigma^A_{xy}/M_S$), quantifying the sensitivity of the magnitude of anomalous Hall current in regard to the magnetization. Inset of Fig. 2(e) illustrates the variation of S_H with temperature, and it remains fairly constant with T at $S_H \approx 0.065$ V^{-1}. This signifies that the observed AHE is immune towards impurity scattering and the deviation in ($\rho^A_{xy}/\rho_{xx}M$) versus ρ_{xx} plot in Fig. 2(d) for the high-temperature regime originates from the variation of magnetization [9,50–52], thus prompting further investigation into the origin of the Berry curvature in k space through *ab initio* calculations.

To understand the impact of magnetism on the electronic structure we have performed spin-polarized calculation in the framework of density functional theory (DFT) using generalized gradient approximation (GGA) by considering the FM and FiM configuration of Mn spins see SM [29] (and Refs. [53–59] therein for method). Our calculations reveal FiM configuration is energetically favorable in comparison to FM configuration. The net magnetic moment of Mn_2PdSn in the ferrimagnetic state is calculated to be 0.48 μ_B. The nearly equal and opposite magnetic moment of 4.54 μ_B and -4.44 μ_B hosted, respectively, by Mn_{4b} and Mn_{4c} atoms in the primitive unit cell of Mn_2PdSn results in a small net moment. The presence of net magnetic moment, although small, breaks the $\mathcal{T}$ symmetry. The spin resolved total and partial density of states for the FiM configuration depict the presence of finite states near Fermi level for both the spin channels, which makes it metallic (Fig. SF5 of SM [29]).

The band structure for the FiM configuration along the high symmetry k-path for Mn_2PdSn is shown in Fig. 3(a). Due to the tetrahedral crystal field, the valance band maxima at the Γ point for both the majority and minority spin channels are threefold degenerate, which are mainly composed of Mn-t_2 states. Along the Γ-L direction, near the Fermi level, the threefold degenerate bands are expected to split into a doubly degenerate and a nondegenerate band, according to the irreducible representation (IRS) of C_{3v} little group. However, due to the absence of $\mathcal{T}$ symmetry in the FiM ground state, the degeneracy is lifted [Fig. 3(b)]. Along Γ-L several band crossings between these nondegenerate bands are observed around the Fermi level.

Next, we have included SOC in our calculation. The calculated energy of Mn_2PdSn in FiM configuration including SOC where the magnetization is along [111] direction is found to be the lowest. Our computational results predict that Mn_2PdSn stabilizes in a noncollinear ferrimagnetic phase where the magnetization axis is along [111] direction. The band structure in the FiM configuration including SOC along [111] direction is shown in Fig. 3(c), where in the presence of SOC the threefold degeneracy at the Γ point is lifted, and several band crossings are observed along the path Γ-L. The band structure along the path Γ-L in a narrow energy range [see Fig. 3(d)] identifies several doubly degenerate points (Weyl points) above the Fermi level. In the spin-orbit coupled band structure along L-Γ-L path, three pairs of Weyl points are located about 100 meV above the Fermi level, and are distinctly seen in Fig. 3(d). The precise position, Chern number, and the chemical potential of these three Weyl points along with some others close to the Fermi level are determined by the iterative

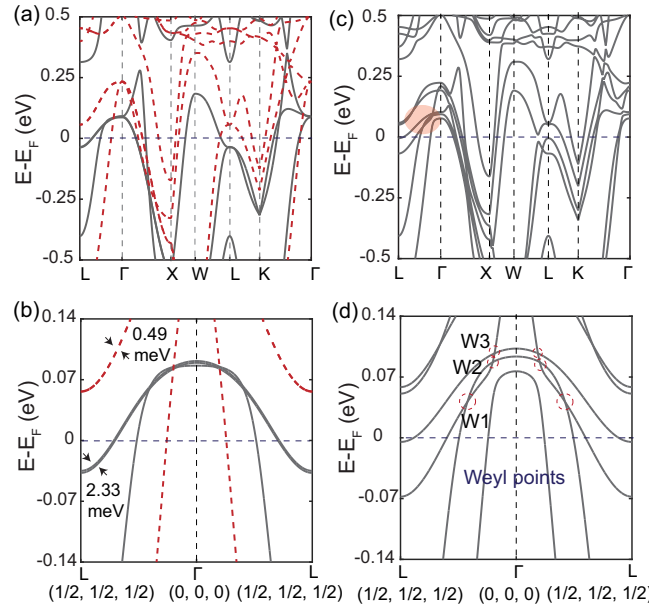

FIG. 3. (a) Spin-polarized band structure of primitive Mn_2PdSn along high symmetry k path for ferrimagnetic (FiM) configuration where up and down spin states are represented with full and dotted lines respectively. The same band structure as in (a) along L-Γ-L path showing nondegenerate nature of the band and their crossings near the Fermi level. (c) Band structure including SOC. The highlighted area in (c) shows several band crossing points. (d) The same band structure as in (c) along L-Γ-L path shows three pairs of Weyl points in the range of ±100 meV. The Fermi level is set at 0 eV.

Green's function approach as implemented in the WannierTools package [58] (Table ST3 of SM [29]). To understand the texture of the three Weyl points along the path Γ-L, we have calculated the normalized Berry curvatures, which indicate the flux at the Weyl point. The normalized Berry curvature shows that a Weyl point either acts as a source, where the flux comes outward from the point (e.g., W1+, W2+, W3+) or sink, where the flux is along the inward direction (e.g., W1−, W2−, W3−), of the Berry curvature, clearly showing the monopole characteristic with definite chirality as illustrated in Figs. 4(a)–4(f).

The Weyl points in the FiM structure are expected to generate finite Berry curvature resulting in transverse anomalous velocity in the electronic motion subsequently producing a large AHC thereby modifying the transport behavior of the compound. The intrinsic AHC ($\sigma_{\alpha\beta}$) is expressed as the integral of the total Berry curvature ($\Omega_{\alpha\beta}$) over the Brillouin zone of the crystal as [60,61], $\sigma_{\alpha\beta} = \frac{e^2}{\hbar}\int_{BZ}\frac{d^3\vec{K}}{(2\pi)^3}\Omega_{\alpha\beta}(\vec{K})$, where $\Omega_{\alpha\beta}(\vec{K}) = \sum_n f_n(\vec{k})\Omega^{\gamma}_n(\vec{k})$ is the sum of the Berry curvatures $\Omega_{n,\alpha\beta}(\vec{K})$ corresponding to the individual bands n, $f_n(\vec{k})$ is the Fermi distribution function and indices (α, β) denote the global cartesian coordinates [60,62]. The Berry curvature can be cast into the form of a Kubo-like formula, which is implemented in the WANNIER90 code [57] as, $\Omega_{n,\alpha\beta}(\vec{K}) = -2i\hbar^2\sum_{m\neq n}\frac{\langle\Psi_{n,\vec{k}}|v_\alpha|\Psi_{m,\vec{k}}\rangle\langle\Psi_{m,\vec{k}}|v_\beta|\Psi_{n,\vec{k}}\rangle}{[E_m(\vec{k})-E_n(\vec{k})]^2}$, where $\Psi_{n,\vec{k}}$ is the Bloch function and $\vec{v}$ is the velocity operator.

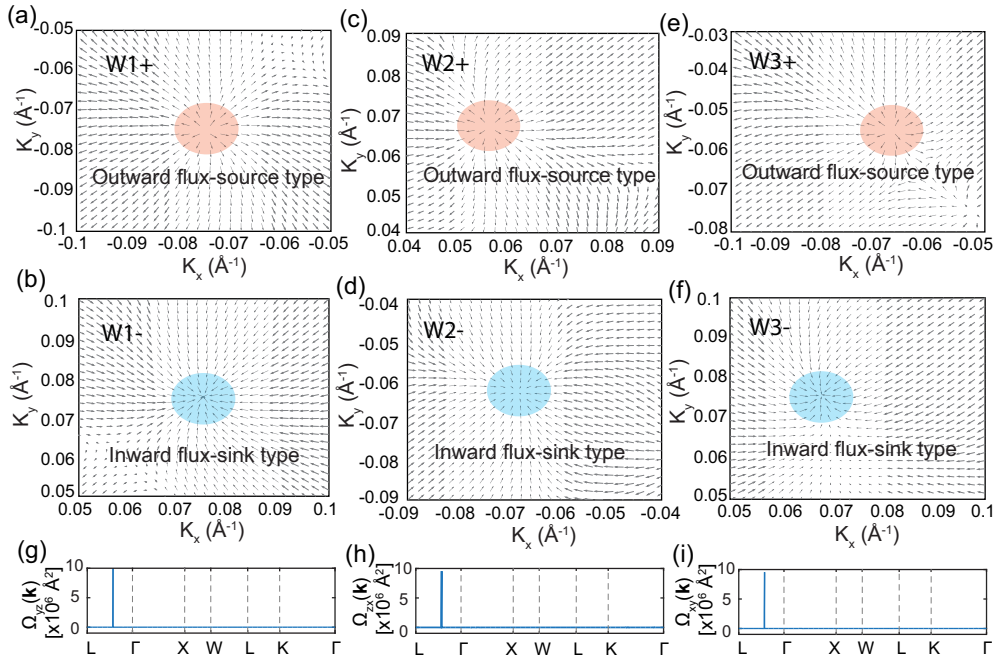

FIG. 4. (a)–(f) Normalized Berry curvature distribution around the Weyl point with positive and negative chirality. (a), (c), (e) Source type assigned by + symbol, which is indicated by outward arrows as highlighted by an orange ellipse. (b), (d), (f) sink type assigned by the − symbol is depicted by inward arrows as emphasized by blue ellipse. (g)–(i) The Berry curvature along the high symmetry k path due to the nontrivial crossings.

The magnetization direction along [111] alters the governing symmetry from cubic to trigonal [63–65]. The symmetry is described by the magnetic space group $R3m'$ (160.67), where the prime denotes the time-reversal symmetry. The resulting constraints imposed on the Berry curvature $\Omega_{\alpha\beta} = (\Omega_{yz}, \Omega_{zx}, \Omega_{xy})$ and therefore, on the AHC $\sigma_{\alpha\beta} = (\sigma_{yz}, \sigma_{zx}, \sigma_{xy})$ by the magnetic space group $R3m'$ can be determined. Notably, the magnetic point group $3m'$ is sufficient to determine the constraints [66,67]. Here, it is worth mentioning that the magnetic mirror symmetry reverses the spin components perpendicular to the magnetic mirror plane and preserves the spin components parallel to the magnetic mirror plane [68]. Therefore, the application of the symmetry operation of the magnetic mirror planes $m'_{10\bar{1}}$, $m'_{01\bar{1}}$, and $m'_{1\bar{1}0}$ preserves the noncollinear ferrimagnetic configuration of Mn_2PdSn.

The above three magnetic mirror planes make all three components of the Berry curvature to be nontrivial hence, the AHC takes the form, $\sigma_{\alpha\beta} = (\sigma_{yz}, \sigma_{zx}, \sigma_{xy})$. Figures 4(g)–4(i) shows the calculated Berry curvature along high symmetry k path. The nonvanishing nature of the three components of the Berry curvature is in agreement with the magnetic symmetry of Mn_2PdSn compound. The peaks in the Berry curvature plot along Γ-L direction originate due to the negligible band separation between the band crossing point. We have calculated three components of the AHC, σ_{yz}, σ_{zx}, and σ_{xy} where x, y, and z axes are considered along [100], [010], and [001] direction of the crystallographic axis. For the magnetization along [111] direction, the AHC tensor can be calculated using another basis where x, y, and z axis are considered along $[\bar{1}10]$, $[\bar{1}\bar{1}2]$, and [111] direction, respectively. The calculated AHC values (shown in Table ST4 of SM [29]), are −58.2, −68.0, and −60.0 S cm^{-1} for σ_{yz}, σ_{zx}, and σ_{xy}, respectively. In the transformed basis the dominant contribution is the $\sigma'_{xy} = -107.4$ S cm^{-1} is in good agreement with the experimentally obtained intrinsic contribution of the AHC value. The value of AHC can be further enhanced by doping so that the energy of the Fermi level is at the Weyl points (see Fig. SF8 of SM [29]).

In conclusion, this comprehensive experimental and *ab initio* investigation highlights the broken inversion symmetry in the iHA system as a conducive environment for realizing bulk Weyl singularities and exploring their associated emergent transport properties. Detailed magnetotransport measurements unveil asymmetric magnetoresistive behavior, primarily originating from domain wall scattering at applied low magnetic fields, resulting in a persistent spin-valve-like effect up to room temperature. Moreover, MR^{asm} exhibits similar temperature and magnetic field variations as magnetization, emphasizing the crucial role of magnetic ordering in the spin-valve effect. A quadratic scaling relation between ρ^A_{xy} and ρ_{xx} is observed, and the calculated AHC resulting from the Berry curvature produced by the Weyl nodes adjacent to the Fermi level closely agrees with the experimentally observed $\sigma^A_{xy,\mathrm{int}}$, confirming the k-space topology as the origin of AHE. Our results underscore the Mn-based iHA with late transition elements at the Y position as a fertile playground for exploring the intricate interplay of noncollinear magnetism and nontrivial electronic band topology. This study further merits the possibility of exploring exotic magnetic functionalities of MWSMs with broken inversion symmetry, such as topological spin-valve technology, owing to the strong correlation between magnetization dynamics and electromagnetic fields mediated by Weyl fermions, through experimental and theoretical investigation for potential applications.

A.B and A.A would like to acknowledge SINP, India and the Department of Atomic Energy (DAE), Government of India for research funding and Fellowship and Soumya Bhowmick for high-temperature measurements. M.R.H. acknowledges Science and Engineering Research Board (SERB), India for providing the financial support through National Post Doctoral Fellowship (NPDF) (Project No. PDF/2021/003366) and Ritwik Das for discussion. I.D. thanks Technical Research Center, Department of Science and Technology (TRC-DST) for the support.

[1] M. Z. Hasan and C. L. Kane, *Colloquium:* Topological insulators, Rev. Mod. Phys. **82**, 3045 (2010).

[2] N. P. Armitage, E. J. Mele, and A. Vishwanath, Weyl and Dirac semimetals in three-dimensional solids, Rev. Mod. Phys. **90**, 015001 (2018).

[3] K. Manna, Y. Sun, L. Muechler, J. Kübler, and C. Felser, Heusler, Weyl and Berry, Nature Rev. Mater. **3**, 244 (2018).

[4] J. F. Steiner, A. V. Andreev, and D. A. Pesin, Anomalous Hall effect in type-i Weyl metals, Phys. Rev. Lett. **119**, 036601 (2017).

[5] H. Weng, C. Fang, Z. Fang, B. A. Bernevig, and X. Dai, Weyl semimetal phase in noncentrosymmetric transition-metal monophosphides, Phys. Rev. X **5**, 011029 (2015).

[6] L. Yang, Z. Liu, Y. Sun, H. Peng, H. Yang, T. Zhang, B. Zhou, Y. Zhang, Y. Guo, M. Rahn *et al.*, Weyl semimetal phase in the non-centrosymmetric compound TaAs, Nature Phys. **11**, 728 (2015).

[7] G. Chang, B. Singh, S.-Y. Xu, G. Bian, S.-M. Huang, C.-H. Hsu, I. Belopolski, N. Alidoust, D. S. Sanchez, H. Zheng, H. Lu, X. Zhang, Y. Bian, T. R. Chang, H. T. Jeng, A. Bansil, H. Hsu, S. Jia, T. Neupert, H. Lin, and M. Z. Hasan, Magnetic and noncentrosymmetric Weyl fermion semimetals in the *R* AlGe family of compounds (R = rare earth), Phys. Rev. B **97**, 041104(R) (2018).

[8] J. Shen, Q. Zeng, S. Zhang, H. Sun, Q. Yao, X. Xi, W. Wang, G. Wu, B. Shen, Q. Liu *et al.*, 33% giant anomalous Hall current driven by both intrinsic and extrinsic contributions in magnetic Weyl semimetal $Co_3Sn_2S_2$, Adv. Funct. Mater. **30**, 2000830 (2020).

[9] K. Kim, J. Seo, E. Lee, K.-T. Ko, B. Kim, B. G. Jang, J. M. Ok, J. Lee, Y. J. Jo, W. Kang *et al.*, Large anomalous Hall current induced by topological nodal lines in a ferromagnetic van der Waals semimetal, Nature Mater. **17**, 794 (2018).

[10] K. Kuroda, T. Tomita, M.-T. Suzuki, C. Bareille, A. Nugroho, P. Goswami, M. Ochi, M. Ikhlas, M. Nakayama, S. Akebi *et al.*, Evidence for magnetic Weyl fermions in a correlated metal, Nature Mater. **16**, 1090 (2017).

[11] L. Ye, M. Kang, J. Liu, F. Von Cube, C. R. Wicker, T. Suzuki, C. Jozwiak, A. Bostwick, E. Rotenberg, D. C. Bell *et al.*, Massive Dirac fermions in a ferromagnetic kagome metal, Nature (London) **555**, 638 (2018).

[12] X. Wan, A. M. Turner, A. Vishwanath, and S. Y. Savrasov, Topological semimetal and Fermi-arc surface states in the electronic structure of pyrochlore iridates, Phys. Rev. B **83**, 205101 (2011).

[13] I. Belopolski, K. Manna, D. S. Sanchez, G. Chang, B. Ernst, J. Yin, S. S. Zhang, T. Cochran, N. Shumiya, H. Zheng *et al.*, Discovery of topological Weyl fermion lines and drumhead surface states in a room temperature magnet, Science **365**, 1278 (2019).

[14] C.-Z. Chang, J. Zhang, X. Feng, J. Shen, Z. Zhang, M. Guo, K. Li, Y. Ou, P. Wei, L.-L. Wang, Z.-Q. Ji, Y. Feng, S. Ji, X. Chen, J. Jia, X. Dai, Z. Fang, S.-C. Zhang, K. He, Y. Wang, L. Lu, X.-C. Ma, and Q.-K. Xue, Experimental observation of the quantum anomalous Hall effect in a magnetic topological insulator, Science **340**, 167 (2013).

[15] C. Shekhar, N. Kumar, V. Grinenko, S. Singh, R. Sarkar, H. Luetkens, S.-C. Wu, Y. Zhang, A. C. Komarek, E. Kampert, Y. Skourski, J. Wosnitza, W. Schnelle, A. McCollam, U. Zeitler, J. Kübler, B. Yan, H.-H. Klauss, S. S. P. Parkin, and C. Felser, Anomalous Hall effect in Weyl semimetal half-Heusler compounds *R*PtBi (R = Gd and Nd), Proc. Natl. Acad. Sci. USA **115**, 9140 (2018).

[16] S. Singh, J. Noky, S. Bhattacharya, P. Vir, Y. Sun, N. Kumar, C. Felser, and C. Shekhar, Anisotropic nodal-line-derived large anomalous Hall conductivity in ZrMnP and HfMnP, Adv. Mater. **33**, 2104126 (2021).

[17] G. K. Shukla, J. Sau, N. Shahi, A. K. Singh, M. Kumar, and S. Singh, Anomalous Hall effect from gapped nodal line in the Co_2FeGe Heusler compound, Phys. Rev. B **104**, 195108 (2021).

[18] A. K. Nayak, V. Kumar, T. Ma, P. Werner, E. Pippel, R. Sahoo, F. Damay, U. K. Rößler, C. Felser, and S. S. Parkin, Magnetic antiskyrmions above room temperature in tetragonal Heusler materials, Nature (London) **548**, 561 (2017).

[19] A. Bhattacharya, A. Ahmed, S. DuttaGupta, and I. Das, Critical behavior and phase diagram of skyrmion-hosting material $Co_{3.6}Fe_{4.4}Zn_8Mn_4$ probed by anomalous Hall effect, J. Alloys Compd. **960**, 170274 (2023).

[20] Y. Venkateswara, J. Nag, S. S. Samatham, A. K. Patel, P. D. Babu, M. R. Varma, J. Nayak, K. G. Suresh, and A. Alam, FeRhCrSi: Spin semimetal with spin-valve behavior at room temperature, Phys. Rev. B **107**, L100401 (2023).

[21] S. Singh, R. Rawat, S. E. Muthu, S. W. D'Souza, E. Suard, A. Senyshyn, S. Banik, P. Rajput, S. Bhardwaj, A. M. Awasthi, R. Ranjan, S. Arumugam, D. L. Schlagel, T. A. Lograsso, A. Chakrabarti, and S. R. Barman, Spin-valve-like magnetoresistance in Mn_2NiGa at room temperature, Phys. Rev. Lett. **109**, 246601 (2012).

[22] S. Agarwal, B. Wang, H. Yang, P. Dhanapal, Y. Shen, J. Wang, H. Wang, J. Zhao, and R.-W. Li, Spin-valve-like magnetoresistance in a Ni-Mn-In thin film, Phys. Rev. B **97**, 214427 (2018).

[23] T. Graf, C. Felser, and S. S. Parkin, Simple rules for the understanding of Heusler compounds, Prog. Solid State Chem. **39**, 1 (2011).

[24] A. A. Zyuzin, S. Wu, and A. A. Burkov, Weyl semimetal with broken time reversal and inversion symmetries, Phys. Rev. B **85**, 165110 (2012).

[25] M. E. Jamer, Y. J. Wang, G. M. Stephen, I. J. McDonald, A. J. Grutter, G. E. Sterbinsky, D. A. Arena, J. A. Borchers, B. J. Kirby, L. H. Lewis *et al.*, Compensated ferrimagnetism in the zero-moment Heusler alloy Mn_3 Al, Phys. Rev. Appl. **7**, 064036 (2017).

[26] R. Stinshoff, A. K. Nayak, G. H. Fecher, B. Balke, S. Ouardi, Y. Skourski, T. Nakamura, and C. Felser, Completely compensated

ferrimagnetism and sublattice spin crossing in the half-metallic Heusler compound $Mn_{1.5}FeV_{0.5}Al$, Phys. Rev. B **95**, 060410(R) (2017).

[27] J. Winterlik, G. H. Fecher, B. Balke, T. Graf, V. Alijani, V. Ksenofontov, C. A. Jenkins, O. Meshcheriakova, C. Felser, G. Liu, S. Ueda, K. Kobayashi, T. Nakamura, and M. Wójcik, Electronic, magnetic, and structural properties of the ferrimagnet Mn_2CoSn, Phys. Rev. B **83**, 174448 (2011).

[28] A. K. Nayak, M. Nicklas, S. Chadov, P. Khuntia, C. Shekhar, A. Kalache, M. Baenitz, Y. Skourski, V. K. Guduru, A. Puri *et al.*, Design of compensated ferrimagnetic Heusler alloys for giant tunable exchange bias, Nature Mater. **14**, 679 (2015).

[29] See Supplemental Material at http://link.aps.org/supplemental/10.1103/PhysRevB.110.014417. This material includes further auxiliary data on structural refinement, transverse resistivity, computational details, and a reference to M. Y. Kharitonov and K. B. Efetov, Hall resistivity of granular metals, Phys. Rev. Lett. **99**, 056803 (2007).

[30] X. Xu, T. Kanomata, M. Hayasaka, R. Umino, K. Endo, H. Nishihara, Y. Adachi, R. Kainuma, and K. R. Ziebeck, Magnetic properties of Mn_2PdSn and Mn_2PdIn, J. Magn. Magn. Mater. **401**, 618 (2016).

[31] L. Feng, X. Feng, E. Liu, W. Wang, G. Wu, J. Hu, and W. Zhang, Possible martensitic transformation in Heusler alloy Mn_2PdSn from first principles, J. Magn. Magn. Mater. **419**, 543 (2016).

[32] S. Onoda, N. Sugimoto, and N. Nagaosa, Quantum transport theory of anomalous electric, thermoelectric, and thermal Hall effects in ferromagnets, Phys. Rev. B **77**, 165103 (2008).

[33] Q. Wang, Y. Xu, R. Lou, Z. Liu, M. Li, Y. Huang, D. Shen, H. Weng, S. Wang, and H. Lei, Large intrinsic anomalous Hall effect in half-metallic ferromagnet $Co_3Sn_2S_2$ with magnetic Weyl fermions, Nature Commun. **9**, 3681 (2018).

[34] P. Li, J. Koo, W. Ning, J. Li, L. Miao, L. Min, Y. Zhu, Y. Wang, N. Alem, C.-X. Liu *et al.*, Giant room temperature anomalous Hall effect and tunable topology in a ferromagnetic topological semimetal Co_2MnAl, Nature Commun. **11**, 3476 (2020).

[35] S. Chatterjee, J. Sau, S. Samanta, B. Ghosh, N. Kumar, M. Kumar, and K. Mandal, Nodal-line and triple point fermion induced anomalous Hall effect in the topological Heusler compound Co_2CrGa, Phys. Rev. B **107**, 125138 (2023).

[36] S. Roy, R. Singha, A. Ghosh, A. Pariari, and P. Mandal, Anomalous Hall effect in the half-metallic Heusler compound Co_2TiX (X = Si, Ge), Phys. Rev. B **102**, 085147 (2020).

[37] G. K. Shukla, J. Sau, V. Kumar, M. Kumar, and S. Singh, Band splitting induced Berry flux and intrinsic anomalous Hall conductivity in the NiCoMnGa quaternary Heusler compound, Phys. Rev. B **106**, 045131 (2022).

[38] E. Cheng, L. Yan, X. Shi, R. Lou, A. Fedorov, M. Behnami, J. Yuan, P. Yang, B. Wang, J.-G. Cheng *et al.*, Tunable positions of Weyl nodes via magnetism and pressure in the ferromagnetic Weyl semimetal CeAlSi, Nature Commun. **15**, 1467 (2024).

[39] N. Shahi, A. K. Jena, G. K. Shukla, V. Kumar, S. Rastogi, K. K. Dubey, I. Rajput, S. Baral, A. Lakhani, S.-C. Lee, S. Bhattacharjee, and S. Singh, Antisite disorder and Berry curvature driven anomalous Hall effect in the spin gapless semiconducting Mn_2CoAl Heusler compound, Phys. Rev. B **106**, 245137 (2022).

[40] S. Chatterjee, J. Sau, S. Ghosh, S. Samanta, B. Ghosh, M. Kumar, and K. Mandal, Anomalous Hall effect in topological Weyl and nodal-line semimetal Heusler compound Co_2VAl, J. Phys.: Condens. Matter **35**, 035601 (2023).

[41] L. Wollmann, S. Chadov, J. Kübler, and C. Felser, Magnetism in cubic manganese-rich Heusler compounds, Phys. Rev. B **90**, 214420 (2014).

[42] R. P. Jena, D. Kumar, and A. Lakhani, Scaling analysis of anomalous Hall resistivity in the Co_2TiAl Heusler alloy, J. Phys.: Condens. Matter **32**, 365703 (2020).

[43] Y. Liu, H. Tan, Z. Hu, B. Yan, C. Petrovic *et al.*, Anomalous Hall effect in the weak-itinerant ferrimagnet $FeCr_2Te_4$, Phys. Rev. B **103**, 045106 (2021).

[44] H. Gu, J. Tian, C. Kang, L. Wang, R. Pang, M. Shen, K. Liu, L. She, Y. Song, X. Liu *et al.*, Sign change of anomalous Hall effect with temperature in $Cr_{2.63}V_{0.25}Te_4$ single crystal, Appl. Phys. Lett. **121**, 191906 (2022).

[45] Q. Wang, S. Sun, X. Zhang, F. Pang, H. Lei *et al.*, Anomalous Hall effect in a ferromagnetic Fe_3Sn_2 single crystal with a geometrically frustrated Fe bilayer kagome lattice, Phys. Rev. B **94**, 075135 (2016).

[46] N. Nagaosa, J. Sinova, S. Onoda, A. H. MacDonald, and N. P. Ong, Anomalous Hall effect, Rev. Mod. Phys. **82**, 1539 (2010).

[47] R. Karplus and J. Luttinger, Hall effect in ferromagnetics, Phys. Rev. **95**, 1154 (1954).

[48] Y. Tian, L. Ye, and X. Jin, Proper scaling of the anomalous Hall effect, Phys. Rev. Lett. **103**, 087206 (2009).

[49] G. Chang, S.-Y. Xu, H. Zheng, B. Singh, C.-H. Hsu, G. Bian, N. Alidoust, I. Belopolski, D. S. Sanchez, S. Zhang *et al.*, Room-temperature magnetic topological Weyl fermion and nodal line semimetal states in half-metallic Heusler Co_2TiX (X = Si, Ge, or Sn), Sci. Rep. **6**, 38839 (2016).

[50] C. Zeng, Y. Yao, Q. Niu, and H. H. Weitering, Linear magnetization dependence of the intrinsic anomalous Hall effect, Phys. Rev. Lett. **96**, 037204 (2006).

[51] Y. Liu, E. Stavitski, K. Attenkofer, and C. Petrovic, Anomalous Hall effect in the van der Waals bonded ferromagnet $Fe_{3-x}GeTe_2$, Phys. Rev. B **97**, 165415 (2018).

[52] G. Gong, L. Xu, Y. Bai, Y. Wang, S. Yuan, Y. Liu, and Z. Tian, Large topological Hall effect near room temperature in noncollinear ferromagnet $LaMn_2Ge_2$ single crystal, Phys. Rev. Mater. **5**, 034405 (2021).

[53] G. Kresse and J. Hafner, *Ab initio* molecular dynamics for liquid metals, Phys. Rev. B **47**, 558 (1993).

[54] G. Kresse and J. Furthmüller, Efficiency of *ab-initio* total energy calculations for metals and semiconductors using a plane-wave basis set, Comput. Mater. Sci. **6**, 15 (1996).

[55] G. Kresse and J. Furthmüller, Efficient iterative schemes for *ab initio* total-energy calculations using a plane-wave basis set, Phys. Rev. B **54**, 11169 (1996).

[56] J. P. Perdew, K. Burke, and M. Ernzerhof, Generalized gradient approximation made simple, Phys. Rev. Lett. **77**, 3865 (1996).

[57] G. Pizzi, V. Vitale, R. Arita, S. Blügel, F. Freimuth, G. Géranton, M. Gibertini, D. Gresch, C. Johnson, T. Koretsune *et al.*, Wannier90 as a community code: new features and applications, J. Phys.: Condens. Matter **32**, 165902 (2020).

[58] Q. Wu, S. Zhang, H.-F. Song, M. Troyer, and A. A. Soluyanov, WannierTools: An open-source software package for novel topological materials, Comput. Phys. Commun. **224**, 405 (2018).

[59] P. E. Blöchl, Projector augmented-wave method, Phys. Rev. B **50**, 17953 (1994).

[60] X. Wang, J. R. Yates, I. Souza, and D. Vanderbilt, *Ab initio* calculation of the anomalous Hall conductivity by Wannier interpolation, Phys. Rev. B **74**, 195118 (2006).

[61] M. G. Lopez, D. Vanderbilt, T. Thonhauser, and I. Souza, Wannier-based calculation of the orbital magnetization in crystals, Phys. Rev. B **85**, 014435 (2012).

[62] D. J. Thouless, M. Kohmoto, M. P. Nightingale, and M. den Nijs, Quantized Hall conductance in a two-dimensional periodic potential, Phys. Rev. Lett. **49**, 405 (1982).

[63] M. Aroyo, J. Perez-Mato, D. Orobengoa, E. Tasci, G. De La Flor, and A. Kirov, Crystallography online: Bilbao crystallographic server, Bulgarian Chemical Communications **43**, 183 (2011).

[64] H. T. Stokes, D. M. Hatch, and B. J. Campbell, Findsym, isotropy software suite, https://iso.byu.edu.

[65] D. M. Hatch and H. T. Stokes, Findsym: program for identifying the space-group symmetry of a crystal, J. Appl. Crystallogr. **38**, 237 (2005).

[66] M. Park, G. Han, and S. H. Rhim, Anomalous Hall effect in a compensated ferrimagnet: Symmetry analysis for Mn_3Al, Phys. Rev. Res. **4**, 013215 (2022).

[67] G. Gurung, D.-F. Shao, T. R. Paudel, and E. Y. Tsymbal, Anomalous Hall conductivity of noncollinear magnetic antiperovskites, Phys. Rev. Mater. **3**, 044409 (2019).

[68] J. Zhou, X. Shu, Y. Liu, X. Wang, W. Lin, S. Chen, L. Liu, Q. Xie, T. Hong, P. Yang, B. Yan, X. Han, and J. Chen, Magnetic asymmetry induced anomalous spin-orbit torque in IrMn, Phys. Rev. B **101**, 184403 (2020).